

Cover Page



Universiteit Leiden



The handle <http://hdl.handle.net/1887/37515> holds various files of this Leiden University dissertation.

Author: Brink, Wyger Maurits

Title: Dielectric shimming : exploiting dielectric interactions in High Field MRI

Issue Date: 2016-01-27

CHAPTER 6

HIGH PERMITTIVITY DIELECTRIC PADS IMPROVE HIGH SPATIAL RESOLUTION MAGNETIC RESONANCE IMAGING OF THE INNER EAR AT 7T

INVEST RADIOL 2014;49:271–277

Wyger M. Brink
Annerie M.A. van der Jagt
Maarten J. Versluis
Berit M. Verbist
Andrew G. Webb

ABSTRACT

Objectives: The objective of this study was to evaluate the use of dielectric pads for improving high spatial resolution imaging of the inner ear at 7T.

Materials and Methods: Two sets of dielectric pads were designed using electromagnetic simulations and implemented using a deuterated suspension of barium titanate. Their effect on transmit efficiency, contrast homogeneity, and diagnostic image quality was evaluated in vivo ($n = 10$). In addition, their effect on the specific absorption rate was evaluated numerically.

Results: Statistically significant improvements ($P < 0.001$) in several measures of the image quality were obtained by using dielectric pads. The dielectric pads lead to an increase in the transmit efficiency and uniformity at the location of the inner ear, which is reflected in both an increased contrast homogeneity and an increased diagnostic value. Simulations show that the dielectric pads do not increase the peak local specific absorption rate.

Conclusion: Using geometrically tailored dielectric pads enables high spatial resolution magnetic resonance imaging of the human inner ear at 7T. The high spatial resolution improves the depiction of the fine inner ear structures, showing the benefit of magnetic resonance imaging at ultrahigh fields.

6.1. INTRODUCTION

Visualization of the fine structures of the inner ear by magnetic resonance imaging (MRI) is of great importance when evaluating patients with sensorineural hearing loss or deafness, vertigo, and tinnitus to identify infectious, inflammatory, and neoplastic disease or congenital malformations [1–5]. Furthermore, there is an increasing interest in anatomical information and normative measures of the inner ear microstructures and the cochlear nerve regarding cochlear implantation. Feasibility of implantation, development of electrodes, and adjustments in operation technique may be guided by these, particularly in cochlear implant surgery with residual hearing preservation (e.g., electroacoustic stimulation) [6–11].

The value of heavily T_2 -weighted magnetic resonance (MR) images for the depiction of the inner ear and internal auditory canal has been recognized since the 1990s when three-dimensional (3D) sequences based on fast spin echo (FSE) or balanced steady-state free precession were introduced. Reported advantages of the FSE technique were reduction of susceptibility artifacts, shorter acquisition time, and maintenance of true T_2 contrast rather than T_2^* contrast of gradient echo sequences [12, 13]. This imaging technique was particularly focused on the visualization of vestibular schwannomas but also provided a good depiction of the inner ear structures. Further improvement of spatial resolution may render a better depiction of the labyrinthine microstructures, particularly in the apex of the cochlea, but attempts to image organs of the membranous labyrinth have been compromised by stop-band artifacts in the case of balanced steady-state free precession sequences and image blurring inherent to FSE sequences [14].

The increased intrinsic signal-to-noise ratio (SNR) afforded by 7T MRI offers an opportunity for improving the depiction of the detailed structures of the inner ear. However, imaging the inner ear at 7T is challenging because of strong inhomogeneities in both the static (B_0) and the transmit radiofrequency (RF; B_1^+) fields, caused by the susceptibility difference between the inner ear fluids and the surrounding bone as well as the elliptical shape of the head, respectively [15]. The B_1^+ nonuniformities in the brain have been studied extensively in neuroimaging at 7T and typically feature areas of low B_1^+ in the temporal lobes, extending down to the temporal bone. The large local B_0 inhomogeneities close to the inner ear suggest that spin echo sequences should be used because of their immunity to resonance frequency offsets; however, their use is limited by the inhomogeneities in the B_1^+ field.

Dielectric pads have previously been used for B_1^+ shimming at 3 and 7T and show potential for improving the B_1^+ distribution without increasing the specific absorption rate (SAR) [16–25]. Suspended metal titanates such as calcium titanate with a relative permittivity of approximately 110 have been used to improve the homogeneity of the B_1^+ field across the brain at 7T [18, 21]. Materials with a higher permittivity, such as suspensions of barium titanate with a relative permittivity of approximately 300, can be used to reduce the required pad thickness because of their stronger interaction with the RF field [22]. These stronger interactions can also be used to increase the B_1^+ locally, albeit at the cost of global B_1^+ homogeneity, while satisfying the geometrical constraints imposed by the close-fitting receiver arrays. This is the mechanism that we aim to exploit in this study to improve the B_1^+ distribution in the inner ear region of interest.

In this work, two sets of dielectric pads, one for male and one for female subjects, are designed using electromagnetic simulations and constructed using a deuterated suspension of barium titanate. The effect of the dielectric pads on SAR is evaluated numerically and their effect on the B_1^+ distribution and image quality is evaluated in vivo. A qualitative comparison of image quality and diagnostic value was performed by two experienced radiologists.

6.2. MATERIALS AND METHODS

ELECTROMAGNETIC SIMULATIONS

Electromagnetic simulations of the transmit RF field were performed using xFDTD (version 7.2; Remcom, Inc, State College, PA) to determine the best geometry of two dielectric pads placed on either side of the head and to assess the effects of these pads on the 10-g averaged SAR distribution. The transmit coil was modeled as a 16-rung high-pass birdcage driven in its fundamental mode using unit voltage sources with an intrinsic impedance of $50\ \Omega$ at the capacitor gaps. The inner diameter of the birdcage was 29.8 cm; each rung was 18.0 cm in length and 2.5 cm in width. The outer diameter of the shield was 35.9 cm and its length was 20.0 cm. The configuration was simulated on a $2.5\ \text{mm}^3$ isotropic grid. Male and female subjects were modeled through “Duke” and “Ella” from the Virtual Family data set, with appropriate tissue parameters assigned to each tissue type [26]. All simulated data were normalized to 1 W of dissipated power in tissue.

The design procedure was set up by defining a baseline geometry for both pads of $10 \times 10\ \text{cm}$ and 1 cm thickness, centered at the ears. The thickness and dielectric properties of the pads were then kept constant, whereas their width and height were varied between 10 and 20 cm in steps of 2 cm to improve the B_1^+ distribution in the inner ear region of interest. The position was finally varied by introducing a positioning offset of up to 5 cm in steps of 1 cm. For each geometry, the B_1^+ distribution was evaluated through a figure of merit formulated in terms of the transmit uniformity, defined as the standard deviation of the B_1^+ divided by its mean value, and the average transmit efficiency, defined as the mean B_1^+ per square root of dissipated power, similar to methods applied earlier in the design of dielectric pads [22–24]. On the basis of this figure of merit, the best geometry was selected for further implementation and evaluation in vivo.

DIELECTRIC PADS

The dielectric pads were constructed using a suspension of barium titanate (–325 mesh powder, Alfa Aesar GmbH & Co. KG, Karlsruhe, Germany) and deuterated water (99.9%, Sigma Aldrich, Zwijndrecht, The Netherlands). Deuterated water was used to suppress the MR signal coming from the dielectric material. The material was characterized using a dielectric probe kit (85070E; Agilent Technologies, Santa Clara, CA) and features a relative permittivity of 286 and electrical conductivity of 0.44 S/m at 298 MHz, which were applied in the electromagnetic simulation model during the numerical design process and SAR evaluation. The mixture was then sealed in polypropylene using a manual sealer (420 SBM-2; Audion Elektro, Weesp, The Netherlands) to form rectangular pads with dimensions outlined later in the article.

MR IMAGING

In vivo experiments were performed on a Philips Achieva 7Tesla system (Philips Healthcare, Best, The Netherlands) using a quadrature transmit/receive birdcage coil (NM008A-7P-012; Nova Medical, Wilmington, MA) and a 32-channel receive array (NMSC075-32-7P; Nova Medical, Wilmington, MA). A series of scans was acquired first with dielectric pads in place and centered on the ears; the pads were then removed, and the entire protocol was repeated for comparison.

Local calibration of the transmit gain was performed by acquiring a whole-head B_1^+ map at a spatial resolution of $2.5 \times 2.5 \times 5 \text{ mm}^3$ using the dual refocused acquisition mode sequence, which takes only 10 seconds to perform [27, 28]. The absence of MR signal coming from the temporal bone obviously limits the accuracy of the B_1^+ estimate in this region; however, an adequate estimate could be obtained from the surrounding tissue. The B_0 field was shimmed to third order using the vendor-supplied image-based shimming routine.

High spatial resolution T_2 -weighted images were acquired both with and without dielectric pads in place using a 3D-FSE sequence with the following sequence parameters: field of view, $180 \times 180 \times 24 \text{ mm}^3$; 0.3 mm^3 isotropic voxels; tip angle/refocusing angle, $90/135^\circ$; time of repetition/time of echo/inter-echo time, 3000/200/12.7 ms, with 69 refocusing RF pulses; parallel imaging in two directions with a reduction factor of 2.5 (left-right) \times 1.5 (feet-head), which resulted in an acquisition time of approximately 10 min. Data were acquired in 10 healthy volunteers (5 females, 5 males; mean age, 25 years). The study was approved by the institution's ethics board, and written informed consent was obtained in all volunteers.

QUALITATIVE IMAGE ANALYSIS

The high spatial resolution T_2 -weighted images obtained with and without dielectric pads were independently scored twice in randomized order by two experienced clinicians (B.V., with 13 years of experience in imaging the temporal bone, and G.H., with 15 years of experience in MRI). The readers were blinded to the subject's name and the acquisition technique used. The contrast homogeneity of the inner ear system, that is, both the right and left inner ears, was rated on a 3-point scale between 1 and 4 as follows: 4, good contrast homogeneity; 2.5, mild contrast inhomogeneity; 1, strong contrast inhomogeneity. The visibility and diagnostic value of the semicircular canals, cochlea, and internal auditory canal (IAC) were rated for both sides individually on a 4-point scale between 1 and 4 as follows: 4, good depiction, high diagnostic value; 3, acceptable visibility, adequate diagnostic value; 2, poor visibility, inadequate diagnostic value; 1, not visible, nondiagnostic image. We note that both ranges were matched to facilitate data interpretation.

STATISTICAL ANALYSIS

Statistical analyses were performed using Statistical Package for the Social Sciences (version 20; IBM, Amsterdam, The Netherlands). To determine the effect of using the dielectric pads, a group analysis was performed per reader by computing the mean score and standard deviation per criteria on the basis of the pooled scores including both observations made. We note that, strictly speaking, a symmetric normal distribution cannot be

assumed given the limited range of the scores; however, this measure gives a reasonable indication of the effect of using the dielectric pads. The scores were debiased on the basis of the acquisition technique used before computing the mean and standard deviations. Statistical differences were determined using a Wilcoxon signed rank test. The intrarater agreement was determined using the Fisher intraclass correlation coefficient and the interrater agreement was determined using the κ coefficient of Cohen. All tests were 2-tailed and $P < 0.001$ was considered to indicate a statistically significant difference.

6.3. RESULTS

ELECTROMAGNETIC SIMULATIONS

The design process of the dielectric pads led to two slightly different configurations for the male and female body models. In the female model, the best pad geometry was found to be a 10×10 cm pad on the left and a 14×14 cm pad on the right side of the head. The male model required a 10×10 cm pad on the left and an 18×14 cm (width \times height) pad on the right side of the head; the difference is caused by the larger male head size. Transverse and coronal cross sections of the resulting simulated transmit efficiency for the four configurations (male/female, with/without pads) are shown in Fig. 6.1. The asymmetric size of the pads is required in both models to correct for the B_1^+ asymmetry at the level of the inner ear when having no pads in place [15]. Simulations of the 10-g averaged SAR distribution show that, for a power normalized case, the local SAR does not increase because of the introduction of the dielectric pads. Maximum intensity projections of the local SAR distribution in the transverse and coronal views are shown in Fig. 6.2.

MR IMAGING

The measured effects of the dielectric pads on the transmit uniformity and efficiency are shown in Fig. 6.3. Transverse maximum intensity projections of the resulting images are shown in Fig. 6.4. It is clear that, without pads, the areas of low B_1^+ overlap almost completely with the inner ear, leading to severe signal dropouts and contrast inhomogeneity. The measured transmit efficiency maps, defined here as B_1^+ over square root of transmitted power, show that the B_1^+ is considerably improved locally by introduction of the dielectric pads, which corresponds to an improved contrast homogeneity throughout the imaging region of interest. We note that the transmitted power includes also power lost in the RF chain, which can be as much as 50% of the total power budget. This introduces an offset between the measured and simulated transmit efficiency maps; because the simulations did not include these losses, however, a relative comparison is still valid.

Remaining small relative differences are most likely caused by differences in the head size and shape of individuals with respect to the model used for the simulations. The left/right asymmetry, which can be observed in the images acquired without pads, is adequately compensated by using a different pad size on either side of the head. Moreover, the images acquired in the male subject reflect the stronger B_1^+ inhomogeneity, which indicates the need for a different pad geometry. It should be noted that the central brightening effect can lead to considerable “overtipping” of the magnetization in the

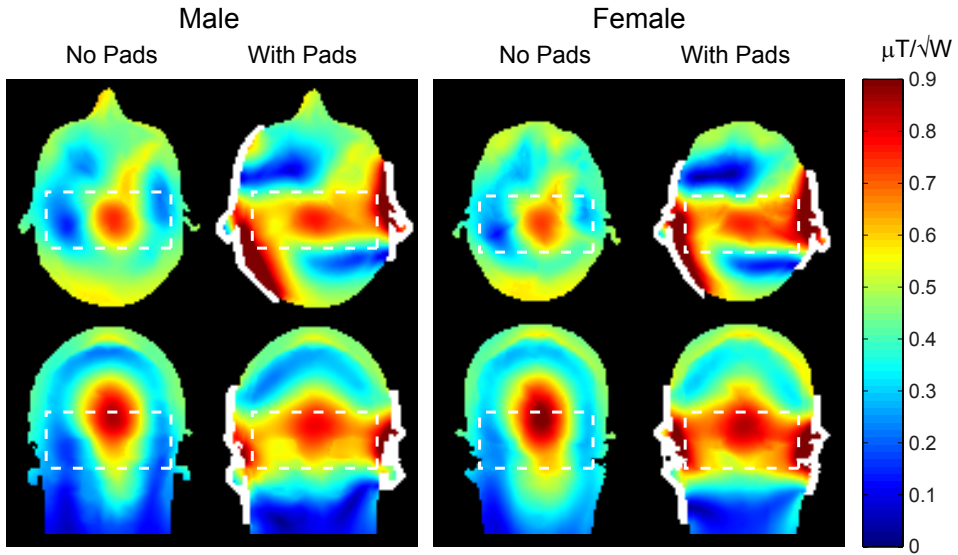


Figure 6.1: Transverse (top) and coronal (bottom) cross sections of the simulated transmit efficiency maps in a male (left) and female (right) body model, without and with dielectric pads. The dielectric pads are illustrated in white and the imaging region of interest of the inner ear is outlined in the dashed box. The maps show the effectiveness of the dielectric pads for locally tailoring the B_1^+ field. The field data are normalized to 1 W of dissipated power in tissue.

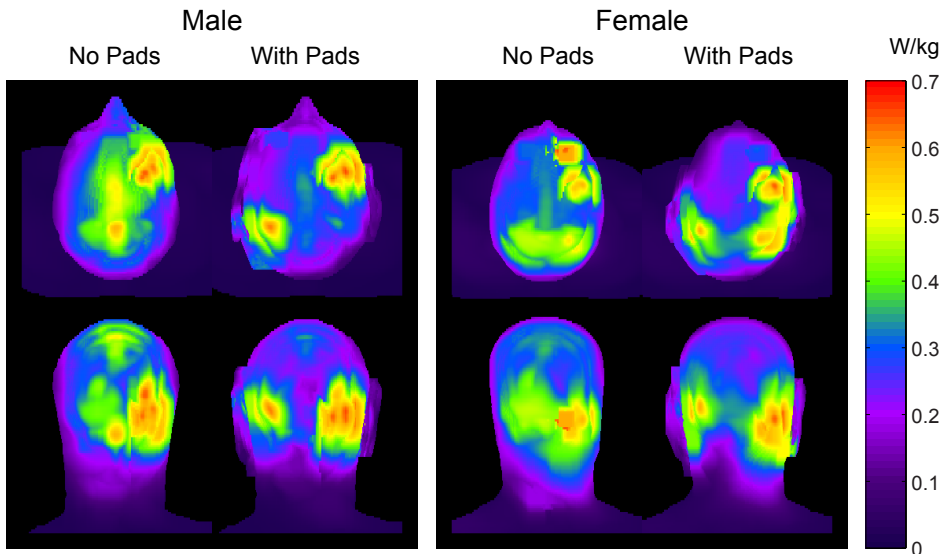


Figure 6.2: Transverse (top) and coronal (bottom) maximum intensity projections of the 10-g averaged SAR distribution for the male (left) and female (right) body model, without and with dielectric pads. Although the dielectric pads change the relative distribution of SAR within the head, they do not lead to an increase in the peak local SAR. All data are normalized to 1 W of dissipated power in tissue.

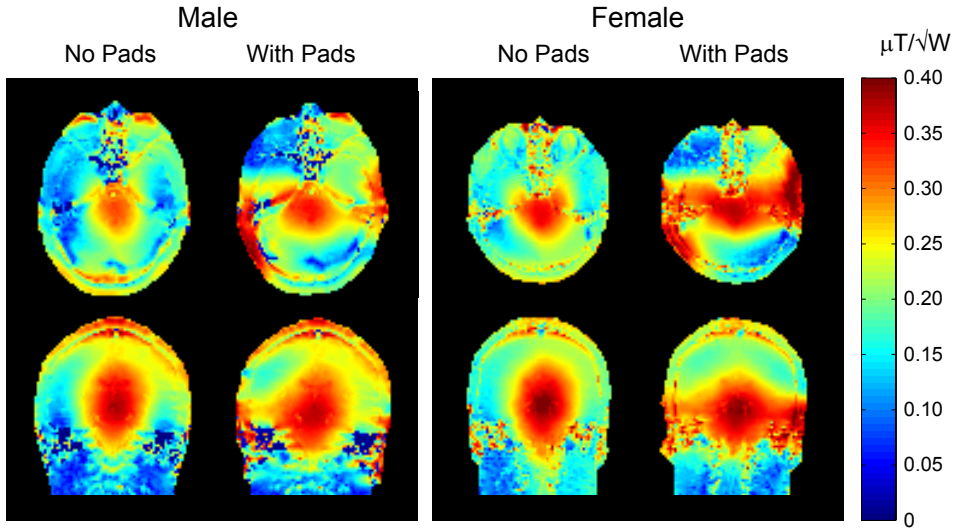


Figure 6.3: Transverse (top) and coronal (bottom) cross sections of the measured transmit efficiency in a male (left) and female (right) subject, without and with dielectric pads. The transmit efficiency maps show the effectiveness of the dielectric pads for locally tailoring the B_1^+ field. The measured field data are normalized to 1 W of transmitted power.

6

center of the brain; that is, the tip angle produced is higher than that which is optimized for the area of the inner ear. This is seen as a slightly reduced signal in the pons with respect to the inner ear.

Figure 6.5 shows multiplanar reconstructions of a high spatial resolution 3D data set, showing the depiction of fine anatomical structures, such as the modiolus, interscalar septum, and spiral osseous lamina. The isotropic voxels allow for oblique multiplanar reconstructions without loss of image quality, which is convenient for visualizing the different branches of the cochleovestibular nerve.

QUALITATIVE IMAGE ANALYSIS

The group results from the qualitative image analysis are presented in Table 1. The dielectric pads improve the mean scores significantly for all criteria evaluated with the exception of the visibility and diagnostic value of the left IAC, for which the image quality without pads was already very high without the dielectric pads. In addition, the dielectric pads improved the consistency of the image quality, which can be seen from the reduced standard deviations.

Intrarater agreement in both readers was good to very good with an intraclass correlation coefficient greater than 0.83. The interrater agreement was moderate to good with a κ value between 0.61 and 0.75.

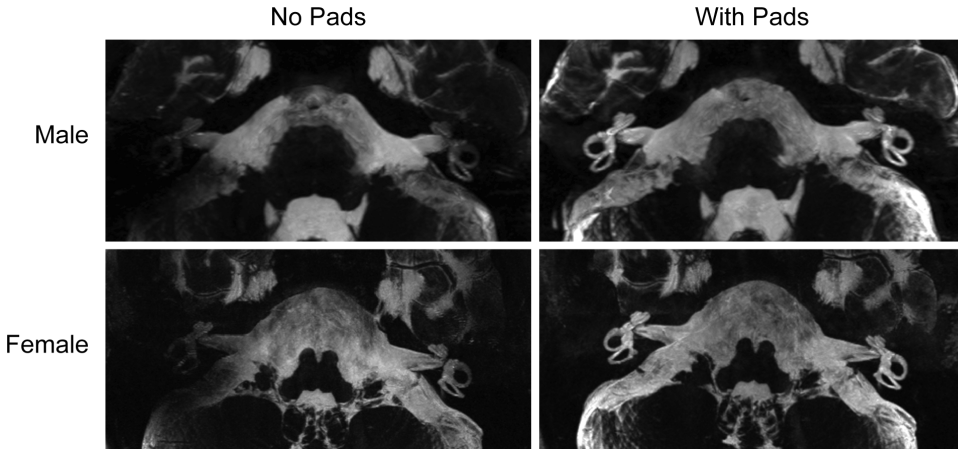


Figure 6.4: Transverse maximum intensity projections of the imaging results for a male (top) and female (bottom) subject, without (left) and with (right) dielectric pads. The introduction of the dielectric pads results in a much improved contrast homogeneity throughout the region of interest.

6.4. DISCUSSION

High spatial resolution MRI of the human inner ear is feasible at 7T by using geometrically tailored dielectric pads, enabling further clinical evaluation of this modality in both anatomical and diagnostic studies. By using dielectric pads filled with suspended barium titanate, which features a high permittivity, the severe B_1^+ inhomogeneities encountered in the temporal bone can be adequately corrected while satisfying the geometrical constraints imposed by the close-fitting 32-channel receiver array. The high spatial resolution improves the depiction of the fine structures of the inner ear, compared with MRI at lower fields, showing the potential benefit from ultrahigh-field MRI.

In this work, we have described two sex-specific geometrical designs for the dielectric pads, for either an average-sized male or female head. In cases wherein the head size deviated substantially from these averages, the design of the pads might have to be altered because the left-right differences in B_1^+ were found to be typically more severe in male subjects with larger head sizes than in female subjects. This trend can also be observed in Fig. 6.4, in which the left inner ear is better depicted in the female subject than in the male subject when no pads are being used.

Whereas imaging at 7T provides a higher intrinsic SNR compared with lower field strength acquisitions, by using a single surface coil for signal reception, scanning at a similar spatial resolution has been performed at 3T [29, 30]. Although a quantitative comparison of SNR has not been performed, the current results indicate that the image SNR at 7T is notably higher. Moreover, the contrast homogeneity is improved at 7T, especially at the IAC, because of the use of the 32-channel receive array instead of a single surface coil for signal reception. Future developments at 7T could incorporate reduced field-of-view imaging techniques to reduce the total imaging time, thereby reducing the potential degradation of the image quality due to physiological or motion-based artifacts [31].

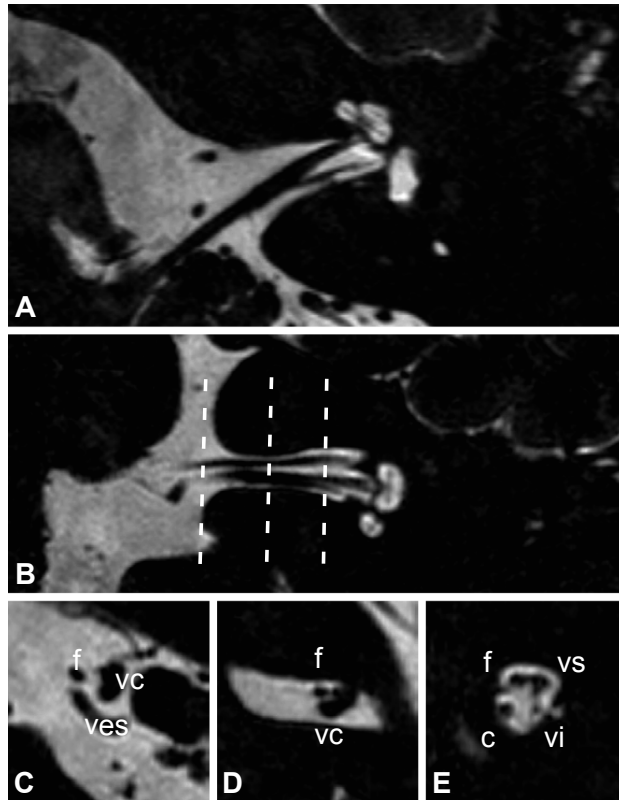


Figure 6.5: Multiplanar reconstructions of a high spatial resolution 3D-FSE data set, in which the depiction of inner ear microstructures can be appreciated (A–B). On reconstructions perpendicular to the internal auditory canal, the different branches of the cochleovestibular nerves are seen (C–E). The approximate locations are indicated by the dashed lines in (B). **c** indicates cochlear nerve; **f**, facial nerve; **vc**, vestibulochochlear nerve; **ves**, vessel (anterior inferior cerebellar artery); **vi**, inferior vestibular nerve; **vs**, superior vestibular nerve.

The geometrical design study indicated that asymmetrically sized pads were required to obtain a symmetric B_1^+ distribution at the level of the inner ear, which is explained by the intrinsic asymmetry observed when no pads are used. This has been consistently observed in vivo and is reproduced in electromagnetic simulations using a realistic numerical head model with inhomogeneous dielectric properties; which implies that this is a fundamental characteristic rather than related to subject positioning or malfunctioning of the RF coil. This B_1^+ asymmetry is known to increase with field strength [32]. Inhomogeneity of B_1^+ , in general, has been studied extensively in the past at various field strengths and has been shown to be related to both the elliptical shape of the phantom and the electrical conductivity of the phantom liquid at 1.5T [15].

The use of dielectric materials for RF shimming has previously been shown to improve the transmit efficacy at high fields, with various applications at 3 and 7T [16–25]. The current work shows that the high permittivity afforded by using barium titanate allows compensation for the strong drop in B_1^+ present in the temporal bone while keeping the pad thickness practical. Care needs to be taken, however, that the field distribution is tailored in the desired way. This can be achieved by considering the initial field distribution, which can be dependent on the subject to a certain degree, and by proper geometrical arrangement of the high dielectric material around the subject. Specifically, a slightly larger pad should be used for male than for female subjects because of the larger head size. This underlines that high permittivity materials offer extended degrees of freedom for tailoring the RF field; however, these need to be addressed with appropriate care.

Correct positioning of the dielectric pads is important to obtain the full advantage of the locally enhanced B_1^+ field. Our approach in this study was to align them centrally with the ears, thus providing an easy anatomical landmark. Furthermore, local calibration of the transmit gain is an important step in obtaining the optimal tip angle at the area of interest, especially given the locally tailored B_1^+ field [33]. After global calibration, which was performed by the scanner in the transverse plane, we observed the estimated tip angle in the petrous bone to vary between 70% and 140% of the target angle because of the inhomogeneous B_1^+ field. Our approach was to obtain an estimate of the B_1^+ magnitude in the petrous bone from measurements of the B_1^+ in the surrounding tissue acquired with the dual refocused acquisition mode method [28]. The advantage of this technique, other than having a very short acquisition time, is its relative independence with respect to relaxation times and resonance frequency offsets. A small error in the B_1^+ estimate in tissues with a very short T_2^* has been observed and analyzed at 7T before; however, this was not a major issue in the current study because the T_2^* of the tissues surrounding the temporal bone is sufficiently long [28]. One remaining source of errors results from the fact that obtaining an estimate of the B_1^+ within the temporal bone was not possible because of the very poor SNR in this area. The accuracy of this may be improved by applying model-based reconstruction methods [34].

An alternative method for B_1^+ shimming at high fields is the use of transmit coil arrays, with dedicated RF signals applied to each channel. Some transmit array designs for imaging the inner ear at 7T have been proposed; however, the additional degrees of freedom present both opportunities as well as challenges with respect to coil implementation and SAR management [35, 36]. Spatially tailored RF pulses can also be used to compensate for B_1^+ inhomogeneities at high field. Although several developments yield

Table 6.1: Group Results of the Qualitative Image Assessment

	Reader A		Reader B	
	No Pads	With Pads	No Pads	With Pads
Contrast Homogeneity	2.0 (0.9)	3.7 (0.5)*	2.0 (0.7)	3.5 (0.6)*
Right ear				
SC	1.9 (0.7)	3.8 (0.4)*	1.8 (1.0)	3.8 (0.4)*
CO	2.4 (0.8)	3.7 (0.5)*	2.2 (1.1)	3.9 (0.3)*
IAC	2.6 (0.9)	3.8 (0.4)*	2.6 (1.0)	4.0 (0.2)*
Left ear				
SC	3.1 (0.6)	4.0 (0.0)*	3.4 (0.6)	4.0 (0.0)*
CO	3.1 (0.6)	3.9 (0.3)*	3.3 (0.7)	4.0 (0.0)*
IAC	3.6 (0.6)	3.7 (0.5)	3.7 (0.5)	4.0 (0.0)

SC indicates semicircular canal; CO, cochlea; IAC, internal auditory canal. Values are expressed as mean (SD). *Significant differences ($P < 0.001$).

promising results in this direction, none of these have yet been applied to high tip angle refocusing pulses of FSE sequences [37, 38]. Adiabatic and composite RF pulses have been applied in two-dimensional FSE and 3D FSE sequences at 7T both for excitation as well as for refocusing and show improvement in the excitation profile; however, this comes at the cost of increased imaging time due to SAR restrictions and increased in-terecho time, limiting the applicability when a 3D imaging volume is required [39, 40]. The advantages of using dielectric pads in this respect are that no additional hardware or software changes are required and that implementation is independent of vendor and platform, which improves the practicality of using this approach. One future improvement would be to combine the dielectric pads with tailored RF pulses. This would be useful for reducing the subject variability of the contrast homogeneity, by compensating for any remaining left-right asymmetry in B_1^+ . Furthermore, tailored RF pulses enable compensation of the area of central brightening, which would improve the contrast homogeneity throughout the pons, for example. We note, however, that, in the clinical setting of inner ear and retrocochlear imaging, the assessment of the brain stem is typically performed by additional sequences that can be optimized separately.

In conclusion, this study shows that in vivo human inner ear imaging is feasible at 7T and that it is significantly improved by using geometrically tailored dielectric pads and renders images with high spatial resolution within reasonable acquisition time. The detailed visualization of the inner ear microstructures as well as cochleovestibular and facial nerve offers opportunities for both anatomical and diagnostic studies. This is of great interest for the development and application of patient-tailored treatment of hearing disorders and vestibular symptoms.

ACKNOWLEDGEMENTS

The authors thank Guido van Haren for his help in scoring the images and Dr. Erik van Zwet for his advice on performing the statistical analyses.

REFERENCES

- [1] Horii A, Kitahara T, Osaki Y, Imai T, Fukuda K, Sakagami M, and Inohara H. Intractable benign paroxysmal positioning vertigo: long-term follow-up and inner ear abnormality detected by three-dimensional magnetic resonance imaging. *Otology & Neurotology* 2010; 31:250–255.
- [2] Verbist BM. Imaging of sensorineural hearing loss: a pattern-based approach to diseases of the inner ear and cerebellopontine angle. *Insights into Imaging* 2011; 3:139–153.
- [3] Carlson M, Van Abel K, Driscoll C, Neff BA, Beatty CW, Lane JI, Castner ML, Lohse CM, and Link MJ. Magnetic resonance imaging surveillance following vestibular schwannoma resection. *The Laryngoscope* 2012; 122:378–388.
- [4] Pyykkö I, Nakashima T, Yoshida T, Zou J, and Naganawa S. Meniere's disease: a reappraisal supported by a variable latency of symptoms and the MRI visualisation of endolymphatic hydrops. *BMJ open* 2013; 3:1–10.
- [5] Wippold, Franz J I, and Turski PA. Vertigo and Hearing Loss. *American Journal of Neuroradiology* 2009; 30:1623–1625.
- [6] Wang G, Vannier MW, Skinner MW, Kalender WA, Polacin A, and Ketten DR. Unwrapping Cochlear implants by spiral CT. *IEEE Transactions on Bio-Medical Engineering* 1996; 43:891–900.
- [7] Sobrinho FP, Yoo HJ, LPR, Lazarini PR, Yoo HJ, de Abreu Júnior L, and Meira AdS. A method for measuring the length of the cochlea through magnetic resonance imaging. *Brazilian journal of otorhinolaryngology* 2009; 75:261–267.
- [8] Herman B, and Angeli S. Differences in cochlear nerve cross-sectional area between normal hearing and postlingually deafened patients on MRI. *Otolaryngology–Head and Neck Surgery* 2011; 144:64–66.
- [9] Fishman AJ. Imaging and anatomy for cochlear implants. *Otolaryngologic clinics of North America* 2012; 45:1–24.
- [10] Gibson D, Gluth MB, Whyte A, and Atlas MD. Rotation of the osseous spiral lamina from the hook region along the basal turn of the cochlea: results of a magnetic resonance image anatomical study using high-resolution DRIVE sequences. *Surgical and radiologic anatomy: SRA* 2012; 34:781–785.
- [11] Kang WS, Hyun SM, Lim HK, Shim BS, Cho JH, and Lee KS. Normative diameters and effects of aging on the cochlear and facial nerves in normal-hearing Korean ears using 3.0-tesla magnetic resonance imaging. *The Laryngoscope* 2012; 122:1109–1114.
- [12] Casselman JW, Kuhweide R, Ampe W, Meeus L, and Steyaert L. Pathology of the membranous labyrinth: comparison of T1- and T2-weighted and gadolinium-enhanced spin-echo and 3DFT-CISS imaging. *American Journal of Neuroradiology* 1993; 14:59–69.

- [13] Naganawa S, Yamakawa K, Fukatsu H, Ishigaki T, Nakashima T, Sugimoto H, Aoki I, Miyazaki M, and Takai H. High-resolution T2-weighted MR imaging of the inner ear using a long echo-train-length 3D fast spin-echo sequence. *European Radiology* 1996; 6:369–374.
- [14] Lane JI, Ward H, Witte RJ, Bernstein MA, and Driscoll CLW. 3-T imaging of the cochlear nerve and labyrinth in cochlear-implant candidates: 3D fast recovery fast spin-echo versus 3D constructive interference in the steady state techniques. *American Journal of Neuroradiology* 2004; 25:618–622.
- [15] Sled JG, and Pike GB. Standing-wave and RF penetration artifacts caused by elliptic geometry: an electrodynamic analysis of MRI. *IEEE Transactions on Medical Imaging* 1998; 17:653–662.
- [16] Yang QX, Mao W, Wang J, Smith MB, Lei H, Zhang X, Ugurbil K, and Chen W. Manipulation of image intensity distribution at 7.0 T: passive RF shimming and focusing with dielectric materials. *Journal of Magnetic Resonance Imaging* 2006; 24:197–202.
- [17] Kataoka M, Isoda H, Maetani Y, Nakamoto Y, Koyama T, Umeoka S, Tamai K, Kido A, Morisawa N, Saga T, and Togashi K. MR imaging of the female pelvis at 3 Tesla: evaluation of image homogeneity using different dielectric pads. *Journal of Magnetic Resonance Imaging* 2007; 26:1572–1577.
- [18] Haines K, Smith NB, and Webb AG. New high dielectric constant materials for tailoring the B1+ distribution at high magnetic fields. *Journal of Magnetic Resonance* 2010; 203:323–327.
- [19] Snaar JEM, Teeuwisse WM, Versluis MJ, van Buchem MA, Kan HE, Smith NB, and Webb AG. Improvements in high-field localized MRS of the medial temporal lobe in humans using new deformable high-dielectric materials. *NMR in Biomedicine* 2011; 24:873–879.
- [20] Yang QX, Wang J, Wang J, Collins CM, Wang C, and Smith MB. Reducing SAR and enhancing cerebral signal-to-noise ratio with high permittivity padding at 3 T. *Magnetic Resonance in Medicine* 2011; 65:358–362.
- [21] Teeuwisse WM, Brink WM, and Webb AG. Quantitative assessment of the effects of high-permittivity pads in 7 Tesla MRI of the brain. *Magnetic Resonance in Medicine* 2012; 67:1285–1293.
- [22] Teeuwisse WM, Brink WM, Haines KN, and Webb AG. Simulations of high permittivity materials for 7 T neuroimaging and evaluation of a new barium titanate-based dielectric. *Magnetic Resonance in Medicine* 2012; 67:912–918.
- [23] de Heer P, Brink WM, Kooij BJ, and Webb AG. Increasing signal homogeneity and image quality in abdominal imaging at 3 T with very high permittivity materials. *Magnetic Resonance in Medicine* 2012; 68:1317–1324.

- [24] Brink WM, and Webb AG. High permittivity pads reduce specific absorption rate, improve B1 homogeneity, and increase contrast-to-noise ratio for functional cardiac MRI at 3 T. *Magnetic Resonance in Medicine* 2014; 71:1632–1640.
- [25] Yang QX, Rupprecht S, Luo W, Sica C, Herse Z, Wang J, Cao Z, Vesek J, Lanagan MT, Carluccio G, Ryu YC, and Collins CM. Radiofrequency field enhancement with high dielectric constant (HDC) pads in a receive array coil at 3.0T. *Journal of Magnetic Resonance Imaging* 2013; 38:435–440.
- [26] Christ A, Kainz W, Hahn EG, Honegger K, Zefferer M, Neufeld E, Rascher W, Janka R, Bautz W, Chen J, Kiefer B, Schmitt P, Hollenbach HP, Shen J, Oberle M, Szczerba D, Kam A, Guag JW, and Kuster N. The Virtual Family—development of surface-based anatomical models of two adults and two children for dosimetric simulations. *Physics in Medicine and Biology* 2010; 55:N23–38.
- [27] Nehrke K, and Börner P. DREAM—A Novel Approach for Robust, Ultrafast, Multi-slice B1 Mapping. *Magnetic Resonance in Medicine* 2012; 68:1517–1526.
- [28] Nehrke K, Versluis MJ, Webb A, and Börner P. Volumetric B1+ Mapping of the Brain at 7T using DREAM. *Magnetic Resonance in Medicine* 2014; 71:246–256.
- [29] Lane JJ, Witte RJ, Bolster B, Bernstein MA, Johnson K, and Morris J. State of the art: 3T imaging of the membranous labyrinth. *American Journal of Neuroradiology* 2008; 29:1436–1440.
- [30] Giesemann AM, Raab P, Lyutenski S, Dettmer S, Bültmann E, Frömke C, Lenarz T, Lanfermann H, and Goetz F. Improved imaging of cochlear nerve hypoplasia using a 3-Tesla variable flip-angle turbo spin-echo sequence and a 7-cm surface coil. *The Laryngoscope* 2014; 124:751–754.
- [31] Wargo CJ, Moore J, and Gore JC. A comparison and evaluation of reduced-FOV methods for multi-slice 7T human imaging. *Magnetic Resonance Imaging* 2013; 31:1349–1359.
- [32] Shajan G, Kozlov M, Hoffmann J, Turner R, Scheffler K, and Pohmann R. A 16-channel dual-row transmit array in combination with a 31-element receive array for human brain imaging at 9.4 T. *Magnetic Resonance in Medicine* 2014; 71:870–879.
- [33] Takahara T, Hoogduin H, Visser F, Naganawa S, Kwee T, and Luijten PR. Imaging of the Inner Ear at 7T: Initial Results. In: *Proceedings of the 18th Annual Meeting of ISMRM, Stockholm, Sweden, 2010*; p. 4448.
- [34] Sbrizzi A, Raaijmakers AJE, Hoogduin H, Lagendijk JJW, Luijten PR, and van den Berg CAT. Transmit and receive RF fields determination from a single low-tip-angle gradient-echo scan by scaling of SVD data. *Magnetic Resonance in Medicine* 2014; 72:248–259.

- [35] Kim KN, Han GC, Heo P, Jeong H, Hong SM, Park JH, Woo MK, Kim YB, and Cho ZH. Potential and Probability of Inner Ear Magnetic Resonance Imaging at 7 T. In: Proceedings of the 21st Annual Meeting of ISMRM, Melbourne, Australia, 2013; p. 2725.
- [36] Kim KN, Heo P, Han GC, Jeong H, Hong SM, Woo MK, Park JH, Kim YB, and Cho ZH. Hybrid RF Coils for Inner Ear Imaging at 7 T MR. In: Proceedings of the 21st Annual Meeting of ISMRM, Melbourne, Australia, 2013; p. 2726.
- [37] Setsompop K, Wald LL, Alagappan V, Gagoski BA, and Adalsteinsson E. Magnitude least squares optimization for parallel radio frequency excitation design demonstrated at 7 Tesla with eight channels. *Magnetic Resonance in Medicine* 2008; 59:908–915.
- [38] Grissom WA, Khalighi MM, Sacolick LI, Rutt BK, and Vogel MW. Small-tip-angle spokes pulse design using interleaved greedy and local optimization methods. *Magnetic Resonance in Medicine* 2012; 68:1553–1562.
- [39] van Kalleveen IML, Koning W, Boer VO, Luijten PR, Zwanenburg JJM, and Klomp DWJ. Adiabatic turbo spin echo in human applications at 7 T. *Magnetic Resonance in Medicine* 2012; 68:580–587.
- [40] Moore J, Jankiewicz M, Anderson AW, and Gore JC. Evaluation of non-selective re-focusing pulses for 7 T MRI. *Journal of Magnetic Resonance* 2012; 214:212–220.